Journal of Electronic Materials (2024) 53:5092–5102
https://doi.org/10.1007/s11664-024-11161-2

28TH INTERNATIONAL CONFERENCE ON NUCLEAR TRACKS AND RADIATION MEASUREMENTS

Metal–Organic Framework (MOF)-Derived SnO_2-ZnO Nanocomposites for Highly Sensitive NO_2 Detection

Shrihari Kannan[1] · Gaurav Pandey[1] · Shiv Dutta Lawaniya[1] · Sanjay Kumar[1,2] · Prashant Sharma[3] · Kamlendra Awasthi[1]

Received: 15 February 2024 / Accepted: 2 May 2024 / Published online: 23 May 2024

Abstract

The presence of nitrogen dioxide (NO_2), a hazardous gas emanating from various sources including vehicles, industrial power plants, indoor combustion appliances, and tobacco smoke, underscores the importance of effective monitoring. Early risk assessment and continuous vigilance are vital to mitigate potential respiratory and cardiovascular consequences associated with prolonged exposure. To address this need, we have developed a cost-effective metal–organic framework (MOF)-derived SnO_2-ZnO-based gas sensor for NO_2 detection. Different combinations of SnO_2-ZnO were synthesized by varying the Sn/Zn molar ratio. The sensor SZ 1–0.5, having Sn/Zn = 1/0.5, demonstrated a superior response (R_g/R_a = 7.37) compared to bare SnO_2 and ZnO towards 100 ppm of NO_2 at 225°C. The fabricated SZ 1–0.5 sensor showed a good response time of 100 s with outstanding selectivity, cyclability, and repeatability. The enhanced gas-sensing characteristics of the sensor are attributed to the formation of heterojunctions. The gas-sensing mechanism is discussed in detail.

Keywords Metal–organic framework · heterojunction · SnO_2 · ZnO · NO_2 · gas sensing

Introduction

In recent years, environmental and health challenges have escalated due to air pollution originating from various sources such as vehicles, industrial activities, etc. The primary culprits contributing to this air pollution include carbon monoxide (CO), nitrogen dioxide (NO_2), sulfur dioxide (SO_2), ozone (O_3), and particulate matter ($PM_{2.5}$, PM_{10}). Continuous exposure to these harmful gases through inhalation presents a significant health concern, leading to various health disease conditions related to the respiratory and cardiovascular system such as lung failure, stroke, and exacerbation of asthma.[1–4] The World Health Organization (WHO) has set the recommended air quality guidelines that include permissible 24-h limits for NO_2 (25 $\mu g/m^3$), SO_2 (40 $\mu g/m^3$), and CO (4 $\mu g/m^3$).[5] Additionally, the National Ambient Air Quality Standard of India has set permissible annual average limits for NO_2 (80 $\mu g/m^3$), SO_2 (60 $\mu g/m^3$), and CO (2 $\mu g/m^3$).[6] Among these harmful gases, Nitrogen dioxide (NO_2) is a prevalent noxious gas. It originates from different sources such as gas exhaust of vehicles and the burning of coal, wood, and oil, etc. Prolonged exposure to NO_2 poses significant health risks, leading to respiratory ailments such as bronchitis, asthma, pulmonary edema, and others.[7–12] In addition, the presence of NO_2 in the atmosphere is also accountable for acid rain and ozone depletion.[10] Hence, there is a requirement for a very precise NO_2 gas sensor with the capability of detecting it at parts per million (ppm) concentrations. Furthermore, in medical applications, the precise detection of small quantities of NO_2 helps in diagnosing chronic lung disease.[13,14]

For NO_2 detection, various sensing materials, including metal—oxide semiconductors (MOS) (ZnO,[15] SnO_2,[16] In_2O_3,[17] etc), carbon-based materials (CNT,[18] graphene,[19,20] graphene oxide,[21] reduced graphene oxide,[22,23] etc.), polymers (polypyrrole,[18,24] polymethyl methacrylate,[25]

✉ Kamlendra Awasthi
kawasthi.phy@mnit.ac.in

1 Department of Physics, Malaviya National Institute of Technology Jaipur, Jaipur, Rajasthan 302017, India

2 CEITEC Brno University of Technology, Brno, Czech Republic

3 CSIR-Central Electronics Engineering Research Institute (CEERI), Pilani, Rajasthan 333031, India

polyaniline,[26] etc.) have been investigated. These materials employ the chemiresistive method for NO_2 gas detection. Among these, MOS-based sensing materials are widely explored for NO_2 sensing and are further categorized into two groups based on their electrical properties: *n*-type MOS and *p*-type MOS. For gas-sensing applications, *n*-type MOS materials are usually preferred over *p*-type MOS due to their significant thermal stability and ability to operate well under lower oxygen partial pressures, whereas *p*-type MOS materials are thermally unstable and tend to exchange lattice oxygen more readily when exposed to air.[27] Among *n*-type MOS, tin oxide (SnO_2) and zinc oxide (ZnO) stand out as promising options due to their cost-effectiveness, non-toxic nature, and ease of synthesis. However, both SnO_2 and ZnO encounter various challenges such as low response levels, poor selectivity, and slow response recovery times in practical NO_2 gas detection applications.[9,11] Addressing these limitations is crucial for enhancing the overall effectiveness and reliability of these MOS in NO_2 gas detection. In recent years, different strategies such as morphological tuning,[28,29] ion doping,[30,31] noble atom decoration,[32,33] and the creation of heterojunctions[34–36] in metal oxides have been employed.

From the morphological tuning perspective, nowadays metal–organic framework (MOF)-derived metal oxides have a strong appeal for gas-sensing applications. MOFs are a promising class of functional materials, having organic ligands and metal ions/clusters interconnected through coordination interactions. Their notable attributes, including high porosity, extensive surface area, diverse composition, and well-defined porous nanostructures, have garnered significant attention from researchers. The metal oxides derived from MOF retain the characteristics of MOF even after calcination, and provide higher and richer active sites and pathways for gas adsorption and diffusion into the sensing material, which enhances their gas-sensing performance.[37–42] In this direction, Bulemo et al. synthesized MOF-derived hollow spheres of SnO_2, which showed a highly selective response ($R_a/R_g = 20.8$) towards 5 ppm of acetone at 350°C. This heightened selectivity was attributed to the extensive surface area and improved porosity of the SnO_2 hollow spheres synthesized from MOF.[43] Ren et al. engineered porous ZnO nanoparticles by utilizing 2-methylimidazole as cross-linkers within a MOF. The resulting ZnO nanoparticles exhibited an increased surface area and featured pores that facilitated gas accessibility. This unique structure contributed to an improved response in the detection of NO_2 gas, evidenced by a notable response ($R_g/R_a = 51.41$) toward 1 ppm of NO_2 at a working temperature of 200°C.[44] Another strategy to enhance the gas sensing characteristics of MOS is the formation of heterojunctions employing *n*–*n*-, *p*–*p*-, or *n*–*p*-type metal oxides. Zhang et al. synthesized an MOF-derived SnO_2-ZnO composite, the composition of which was varied by adjusting the different molar concentrations (5–20%) of SnO_2 to ZnO; 6% SnO_2-ZnO showed the highest response ($R_a/R_g = 140.27$) at 240°C towards 10 ppm of acetone, which is 40% higher than bare ZnO.[45] The *n*–*n* heterostructure facilitated the electron transfer, which resulted in a superior sensing response. Cheng et al. synthesized an MOF-derived SnO_2-ZnO nanocomposite. This nanocomposite demonstrated an amplified response ($R_a/R_g = 51$) when exposed to 100 ppm of ethanol at an operational temperature of 160°C, which was five times greater than that observed with the unmodified SnO_2. The enhanced performance was attributed to the synergistic effects of combining SnO_2 and ZnO in the nanocomposite structure.[37] GuO et al. synthesized a Pt-ZnO-In_2O_3 composite involving an MOF-based synthesis route. The gas-sensing response ($R_a/R_g = 57.1$) towards 100 ppm of acetone at 300°C was improved by the formation of *p*–*n* (PtO_2-ZnO) and *n*–*n* heterojunctions (ZnO-In_2O_3), compared to bare In_2O_3 and ZnO-In_2O_3 alone.[46]

In this direction, we have synthesized an SnO_2-ZnO nanostructure by utilizing 2-methylimidazole as cross-linkers. To assess the impact of different Zn mole ratios to Sn on the gas-sensing properties of SnO_2-ZnO, we prepared various combinations of SnO_2-ZnO through solution phase synthesis, by varying different Zn molar ratios to Sn. The SnO_2-ZnO (SZ 1-0.5) having Sn/Zn in the molar ratio of 1/0.5 showed the highest response toward NO_2 gas at a temperature of 225°C.

Experimental

Materials

Tin chloride (V) pentahydrate ($SnCl_4.5H_2O$; Himedia, 98.0%), zinc nitrate hexahydrate ($Zn(NO_3)_2{\cdot}6H_2O$; Loba Chem, 98%), and 2-methylimidazole (2-HmIm; Loba Chem, 98%) were used as precursors. Methanol (Rankem, 99%) was used as a solvent, and α-terpineol (Alfa Aesar, 99%) was used as a binder.

Synthesis of MOF-Derived SnO_2-ZnO Nanostructures

For the synthesis of the SnO_2-ZnO nanocomposite, typically, 24.7 mmol of $SnCl_4{\cdot}5H_2O$ was combined with specific quantities (0, 6.175 mmol, 12.35 mmol, 18.52 mmol, and 24.7 mmol) of $Zn(NO_3)_2{\cdot}6H_2O$ in the molar ratios of Sn/Zn of 1/0, 1/0.25, 1/0.50, 1/0.75, and 0/1, in 60 ml of methanol. After proper mixing of the precursor, 98.7 mmol of 2-HmIm (2-methylimidazole) was added to the solution, resulting in a light transparent solution. The solution was allowed to mixed for 2 h. After the stirring stopped, the solution was allowed to age for 20 h, which changed the transparent solution into a whitish solution. The resultant precipitate was thoroughly washed with methanol multiple times and subsequently

dried at 60°C for 12 h. Following the drying process, the metal–MOF complex was ground in a mortar and pestle and subsequently annealed at 450°C in an air furnace for 3 h.

Material Characterization

The crystal structure and composition of the synthesized sample were analyzed using an X-ray diffractometer (XRD) having Cu Kα_1 ($\lambda = 1.54$ Å) as the source. A field-emission scanning electron microscope (FESEM; Nova Nano FESEM 450; FEI) was utilized to morphologically analyze the synthesized sample. A Keithley source meter (SMU 2601b) was used for resistance measurement and a Keithley 2260 for the DC power supply.

Sensor Fabrication and Sensing Measurement

For sensor fabrication, aluminum interdigitated electrodes (IDEs) were applied onto a SiO_2/Si substrate, possessing a thickness of 400 μm and a gap of 200 μm between the electrode fingers. The synthesized samples were transformed into a slurry in a mortar and pestle, incorporating a few drops of α-terpineol. Subsequently, this slurry was applied to the IDEs and dried in an oven at 60°C for 6 h. Gas-sensing measurements were conducted within a self-made testing chamber regulated by the LabView program, which facilitated communication between the various components. The resistance of the fabricated sensor was measured using the Keithley source meter, while temperature control within the testing chamber was regulated by the Keithley DC power supply. To regulate the flow of both dry air (comprising 80% N_2 and 20% O_2) and the target gas, two mass flow controllers (MFCs) were used. The intended concentration of the target gas was attained by mixing the 1000 ppm of the gas with the dry air using the MFC. The response of the fabricated sensor was then calculated using:[47–51]

$$\text{Response} = \frac{R_g}{R_a}$$

where R_a represents the sensor resistance in a dry air atmosphere and R_g represents the sensor resistance in the presence of the target gas. A schematic illustrating the synthesis process of the material and gas-sensing measurement is presented in Fig. 1.

Results and Discussion

Material Characterization

XRD analysis was utilized to investigate the crystal structure and phase formation of the synthesized samples, as depicted in Fig. 2. The observed spectra of bare SnO_2 (S1-0) and bare ZnO (S0-1) matches the standard tetragonal phase of SnO_2 (JCPDS 01-0657) and the hexagonal wurtzite phase of ZnO (JCPDS 36-1451), respectively.[47,49] This indicates the formation of pure phases in the bare samples, devoid of any impurity phases. In the XRD patterns of the SnO_2-ZnO samples (SZ 1–0.25, SZ 1–0.50, SZ 1–0.75), the diffraction peaks aligned with those of bare SnO_2. The dominance of SnO_2 diffraction peaks is observed due to the smaller molar contribution of ZnO compared to SnO_2.

The average crystallite size of the synthesized samples was calculated using the Debye–Scherrer equation:[47]

$$D = \frac{K\lambda}{\beta \cos\theta}$$

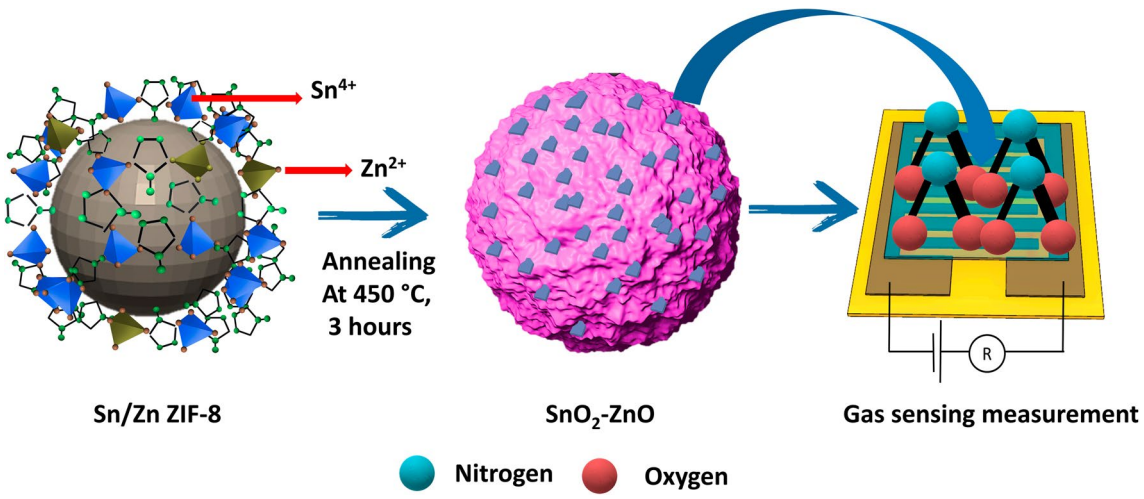

Fig. 1 A graphical representation of SnO_2-ZnO synthesis and gas-sensing setup.

where λ represents the wavelength of Cu Kα_1 ($\lambda = 1.54$ Å), K is the shape factor constant (= 0.9), β is the full width half-maxima, and θ is the diffraction angle. The average crystallite size calculated 2.88 nm, 4.60 nm, 5.76 nm, 8.73 nm, and 16.69 nm for SZ 1–0, SZ1–0.25, SZ 1–0.50, SZ 1–0.75, and SZ 0–1 respectively. The larger crystalline size observed in the ZnO is attributed to its inherently higher crystallinity, whereas the SnO_2-based samples exhibit lower crystallinity with broader peaks.

Furthermore, the morphological characterization of SnO_2, ZnO, and SnO_2-ZnO was carried out through FESEM, as shown in Fig. 3. The FESEM images of bare SnO_2 (Fig. 3a) show a spherical shaped morphology with a rough surface and have an average particle size of 0.74 μm, while the bare ZnO (Fig. 3b) shows an assembly of smaller nanoparticles with an average particle size of 64.16 nm. The introduction of ZnO to the SnO_2 results in mixed nanostructures having smaller nanoparticles on the surface of large spherical nanostructures (Fig. 3c) with an average particle size of 1.43 μm, suggesting an outer decoration of SnO_2 with the ZnO nanostructures. These particle sizes are different from the crystallite size observed in XRD because the observed particle size being due to the agglomeration of many crystallites. The material having smaller crystallites has a large surface free energy, which tends to agglomerate faster and grow into large grains.[52] The elemental mapping conducted on a small cross-sectional area, depicted in Fig. 3d, reveals a consistent distribution of Sn, Zn, and O elements across the surface, which are consistent with the findings of XRD.

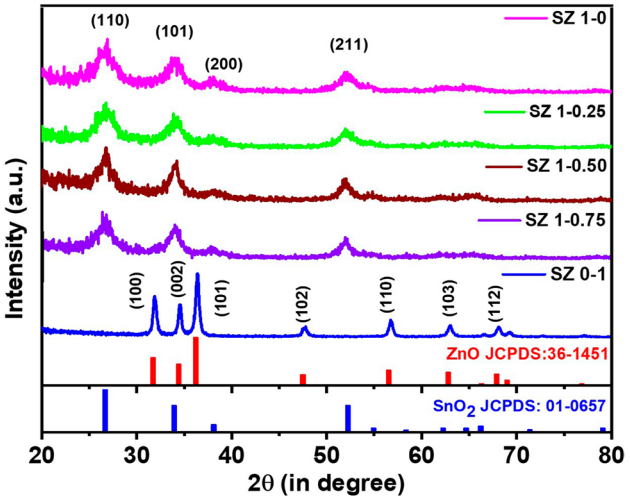

Fig. 2 XRD spectra of MOF-derived SnO_2-ZnO.

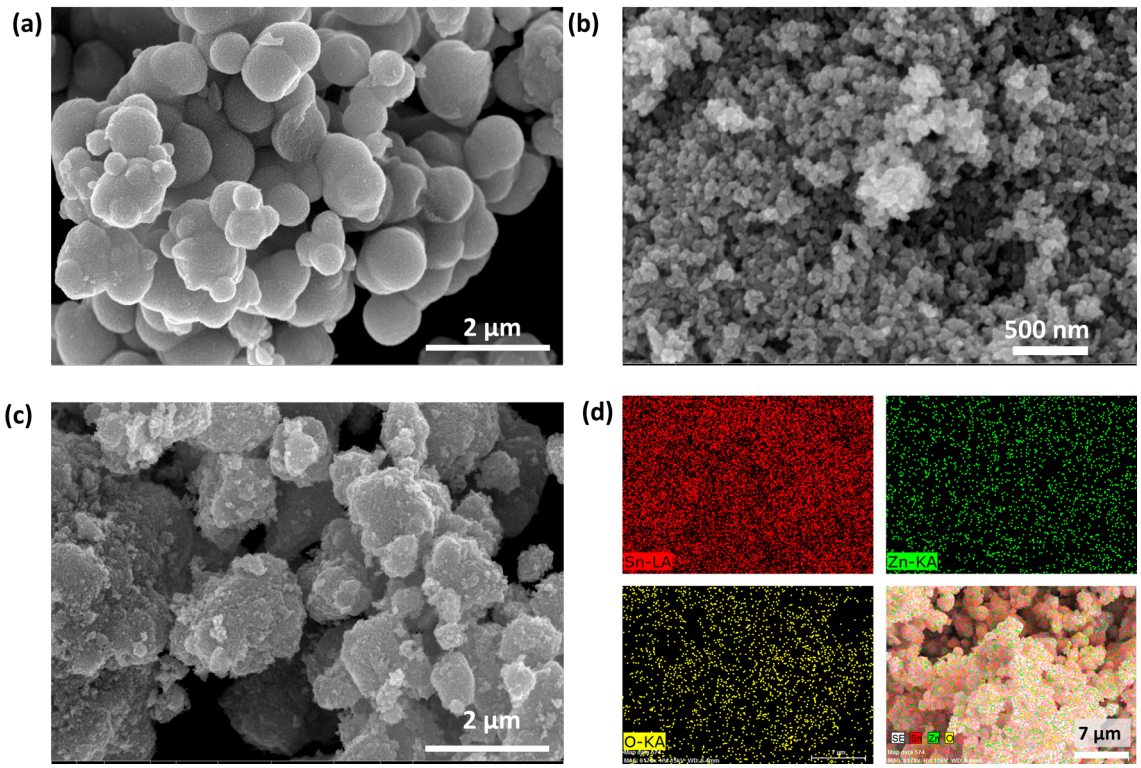

Fig. 3 FESEM images of (a) bare SnO_2 (SZ 1–0), (b) bare ZnO (SZ 0–1), and (c) SnO_2-ZnO (SZ 1–0.50), and (d) elemental distribution mapping of SnO_2-ZnO (SZ 1–0.50) for elements Sn, Zn, and O.

Gas-Sensing Results

The gas-sensing performance of the fabricated sensors was assessed towards 100 ppm of NO_2 at different temperatures, as shown in Fig. 4a. The molar ratio of Sn/Zn was found to play a crucial role in the sensor performance towards NO_2 gas. For bare SnO_2 (SZ 1–0) and ZnO (SZ 0–1), only their outer surfaces react with NO_2, resulting in a weaker sensing response. When ZnO is introduced to SnO_2, a SnO_2-ZnO heterojunction was formed; however, the low proportion of ZnO limits its contribution to sensing. Further, when the ZnO contribution was increased with a molar ratio of Sn/Zn = 1/0.5, the highest sensor response (R_g/R_a) of 7.37 was achieved at 225°C. This peak response was attributed to optimized surface interactions of NO_2 with SnO_2, ZnO, and SnO_2-ZnO heterojunctions. An increase in the molar concentration of ZnO could lead to ZnO nanoparticles covering the SnO_2, thereby diminishing the contributions from both bulk SnO_2 and the SnO_2-ZnO heterojunction, which ultimately causes a decline in the sensing response. A prior study conducted by Ren et al. also demonstrated that the ZnO:SnO_2 molar ratio influences the gas-sensing response, with the optimal response observed at a ZnO:SnO_2 molar ratio of 2:1.[53] The observed trend of sensor response with temperature shown in Fig. 4a exhibits a rising trend as the temperature increases to a particular temperature of 225°C, after which it begins to decline. This could be attributed to the lower temperature causing insufficient activation energy for the NO_2 gas to react with the adsorbed oxygen species. As the temperature rises, both the physical and chemical adsorption of NO_2 increases, leading to an enhanced response up to 225°C. Beyond this temperature, the desorption rate of NO_2 gas surpasses its adsorption rate, resulting in a decrease in response. Furthermore, the variation of baseline resistance of fabricated sensors with temperature was examined, as shown in Fig. 4b. A consistent decrease in resistance was observed across all the sensors as the temperature increased. This trend could be attributed to fluctuations in the number of charge carriers within the sensing material. Elevated temperatures enhance the intrinsic excitation of MOS semiconductors, resulting in a generation of more charge carriers and subsequently leading to a decrease in resistance.[48,54]

Figure 5a depicts the change in baseline resistance in both dry air and 100 ppm NO_2 environment at an operating temperature of 225°C. The baseline resistance shows the lowest resistance of bare SnO_2 (SZ 1–0). However, as ZnO is introduced to SnO_2, an increase in resistance is observed, possibly due to the formation of a heterojunction. When NO_2 gas is exposed, the most significant change in resistance is found in SZ 1–0.5, suggesting that NO_2 efficiently extracts electrons from the surfaces of SnO_2, ZnO, and the SnO_2-ZnO heterojunction, as previously discussed.[53] The dynamic resistance curve of the SZ 1–0.50 sensor at 225°C is shown in Fig. 5b for a range of NO_2 gas concentrations (25–100 ppm). Upon exposure to NO_2 gas, the resistance of the sensor increased, which is the typical *n*-type semiconductor behavior in the presence of oxidizing gas.[15] Furthermore, as the concentration of the analyte gas rises, the corresponding increase in resistance is observed. This phenomenon can be attributed to the increased availability of analyte molecules interacting with active sites on the sensor's surface during periods of gas exposure, particularly evident at higher concentrations compared to lower ones.[47] The response and recovery times of the sensor are defined as the time interval to obtain 90% of the total signal changes during the adsorption and desorption of the analyte gas.[49] The response and recovery times of the SZ 1–0.5 sensor were found to be 100 s and 440 s, respectively, as shown in Fig. 5c. The response and recovery times of gas sensors are intricately linked to multiple factors. These factors include the diffusion kinetics of analyte gas molecules within the

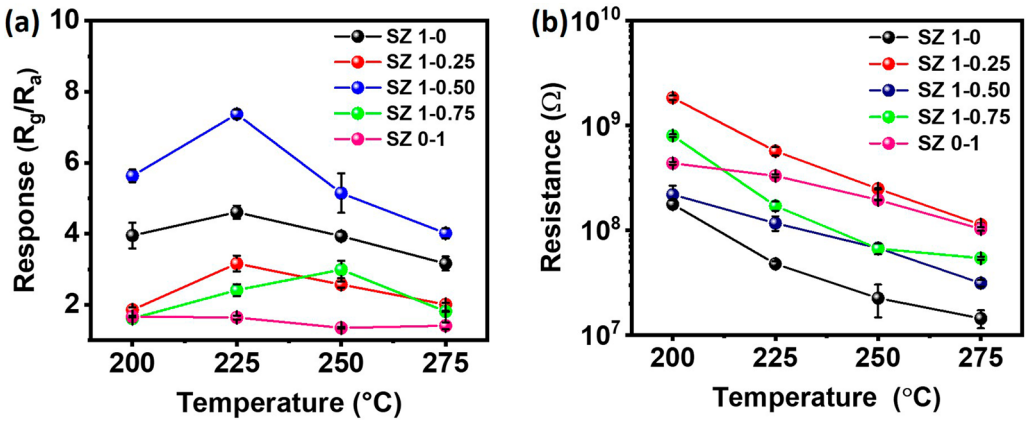

Fig. 4 (a) Response variation, and (b) baseline resistance variation with temperature for the SnO_2-ZnO sensor.

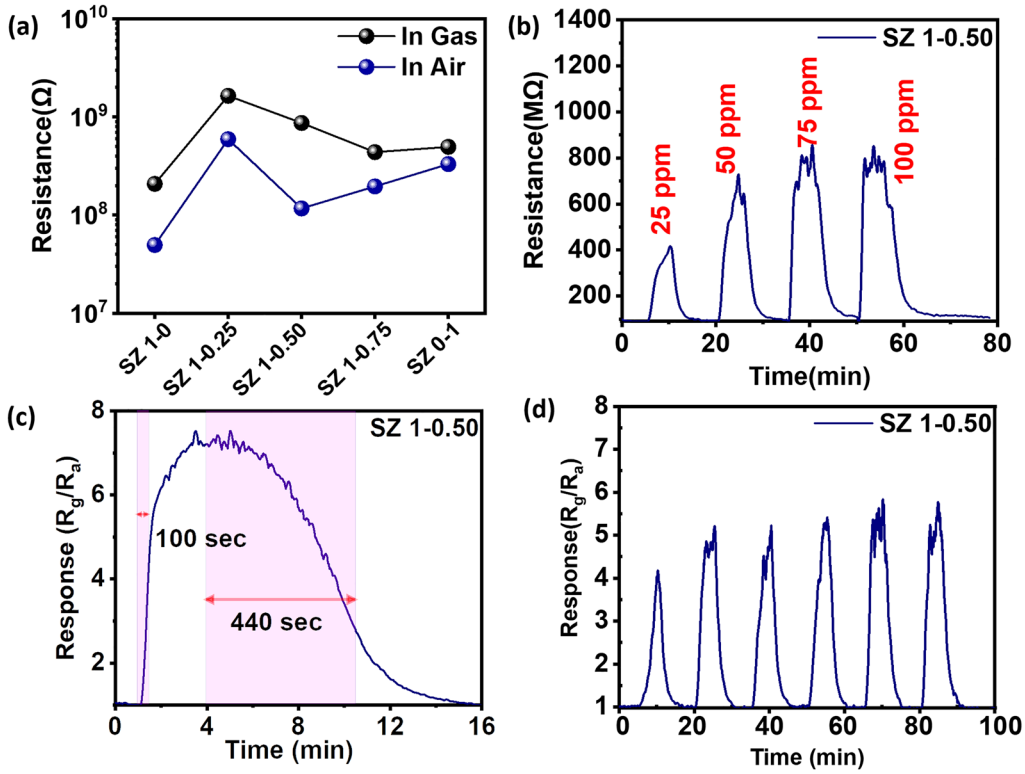

Fig. 5 (a) Resistance variation of the fabricated sensors in air and 100 NO_2 gas at 225°C, (b) dynamic resistance curve of SZ 1–0.50 for NO_2 gas concentration (25–100 ppm) at 225°C, (c) response–recovery of SZ 1–0.50 sensor at 225°C for 100 ppm of NO_2, and (d) cyclability of SZ 1–0.50 sensor towards 25 ppm of NO_2 at 225°C.

sensing material, their affinity to interact with the sensing material, the morphology and particle size of the sensing material, and the experimental parameters such as atmospheric conditions, operating temperature, and gas chamber design (volume, gas flow direction, and flow type).[55–57] In our case, the slow desorption of adsorbed gases due to the thick deposited material, the agglomerated nature of the sensing materials, which leads to increased resistance to electron conduction at grain boundary contacts, and the design of the gas chamber might be the reason for such prolonged response and recovery times.[47,48,58] The repeatability of the fabricated sensor is a crucial aspect for practical applications. To assess this, the cyclability of the SZ 1–0.5 sensor was tested with 25 ppm NO_2 gas for 5 cycles, as illustrated in Fig. 5d. The response of the sensor shows minimal variation, with a standard deviation of ±0.41, underscoring the excellent repeatability of the sensor.

Assessing the long-term stability of the sensor is paramount, and, in this context, the response of the SZ 1-0.50 sensor was monitored over 3 weeks, as shown in Fig. 6a. The results exhibited a negligible change in response, underscoring the excellent stability of the fabricated sensor over a 3-week duration. To evaluate the selectivity of the fabricated sensor, gas-sensing measurements of SZ 1–0.50 were conducted at 225°C using 100 ppm of various gases, including hydrogen, ammonia, and ethanol, as shown in Fig. 6b. The SZ 1–0.50 sensor showed a prominent response ($s = R_g/R_a$) of 7.37 when exposed to 100 ppm of NO_2, whereas it displayed notably lower responses to 100 ppm of other gases, including ethanol (1.70), ammonia (1.28), and hydrogen (1.30). The higher selectivity of SZ 1–0.5 for NO_2 compared to other interfering gases is due to the higher electron affinity of NO_2 as it is more inclined to extract electrons from the SnO_2, ZnO, and SnO_2-ZnO heterojunction.[44]

Finally, for a better comparison of the findings, we compared our data with recent literature, as shown in Table I.

Gas-Sensing Mechanism

The gas-sensing mechanism of SnO_2 and ZnO follows *n*-type semiconductor behavior. Upon exposure of the SZ 1–0 and SZ 0–1 sensors to the air, oxygen molecules adsorb onto the surfaces of SnO_2 and ZnO, leading to the formation of distinct oxygen species, namely O_2^- and O^-. In this process, electrons are extracted from the conduction bands of SnO_2 and ZnO, leading to the formation of a depletion layer on their surfaces. Upon subsequent exposure to NO_2, the sensor extracts electrons from SnO_2 and

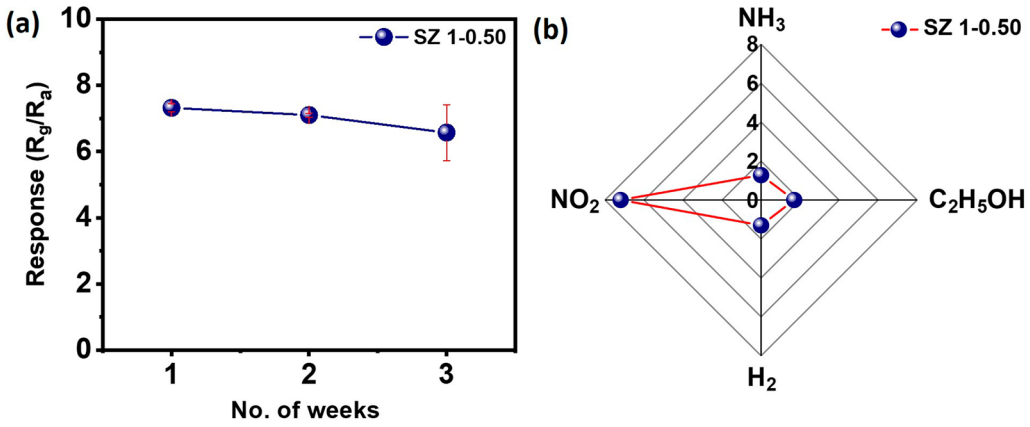

Fig. 6 (a) Long-term stability of SZ 1–0.50 towards 100 ppm of NO_2 gas for 3 weeks at 225°C, and (b) selectivity of SZ 1–0.5 sensor towards 100 ppm of NO_2, H_2, C_2H_5OH, and NH_3 at 225°C.

Table I A comparison of previous reported MOS heterostructure-based NO_2 gas sensors

Material	Morphology	Working temp (°C)	Concen. (ppm)	Response	Response/recovery time (s)	References
CuO/ZnO	Nanowire	250	100	4.1[a]	25/150	59
TiO_2/ZnO	Nanowire	200	5	7[b]	65/98	60
Defect SnO-SnO_2	Nanosheet	150	50	100[c]	10.69/5.83	34
SnO_2-Sn_3O_4	Microsphere	150	50	940[b]	25/14	61
NiO-SnO_2	Nanoweb	300	10	36[b]	163/204	35
CuO-ZnO	Nanowire	150	100	175[d]	14/197	62
ZnO-TiO_2	Nanorods	180	100	350[b]	14/6	63
SnO_2-ZnO	Microsphere	225	100	7.34[b]	100/440	This work

$a = R_a/R_g$, $b = R_g/R_a$, $c = (R_a–R_g)/R_a$, $d = \left|\left(R_a - R_g\right)/R_a\right| \times 100$.

ZnO, causing a further expansion of the depletion layer and an increase in resistance, as illustrated in Fig. 7a. During the recovery phase in air, electrons are transferred back to the conduction band of SnO_2 and ZnO, restoring the depletion layer to its initial state.[64,65] This restoration process brings the resistance back to its initial value. The overall formation of the oxygen species is as follows:

$$O_2 \rightarrow O_2$$

$$O_2 + e^- \rightarrow O_2^-$$

$$O_2 + e^- \rightarrow 2O^-$$

When the sensor is exposed to NO_2, the sensing mechanism is as follows:

$$NO_2 + e^- \rightarrow NO_2^-$$

$$NO_2 + e^- \rightarrow NO + O^-$$

$$NO_2^- + O_2^- + 2e^- \rightarrow NO_2^- + 2O^-$$

$$NO_2^- + O^- + 2e^- \rightarrow NO + 2O^{2-}$$

The formation of heterojunctions between SnO_2 and ZnO also contributes to the overall gas-sensing response. As both SnO_2 and ZnO have different electron affinity ($\chi = 4.5$ eV for SnO_2, $\chi = 4.3$ eV for ZnO), band gaps ($E_g = 3.6$ eV for SnO_2, $E_g = 3.4$ eV for ZnO), and work functions ($\varphi = 4.9$ eV for SnO_2, $\varphi = 5.2$ eV) and Fermi energy levels of SnO_2 are higher than the ZnO.[64,66] So, when the nanograins of SnO_2 and ZnO come into contact with each other an electron transfer takes place from a higher Fermi level (SnO_2)

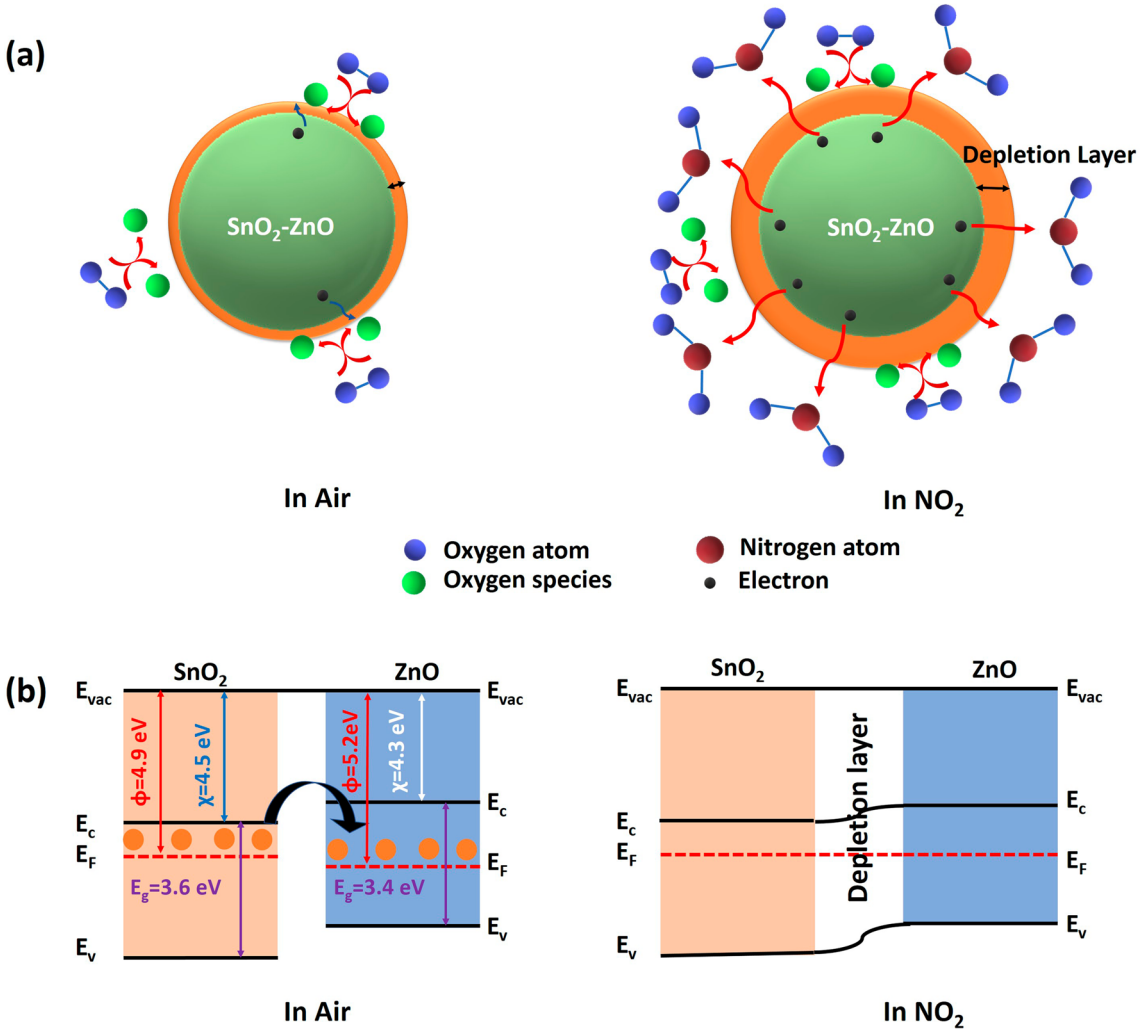

Fig. 7 (a) Schematic of gas-sensing mechanism of SnO_2-ZnO in dry air and NO_2 environment, (b) schematic of energy band structure of SnO_2-ZnO in dry air and NO_2 environment.

to a lower Fermi level (ZnO) until equalization of the levels. This results in an increasing electron accumulation layer in the ZnO side interface and an electron depletion layer in the SnO_2 side interface. This charge layer discontinuity between the SnO_2 and ZnO results in the formation of heterojunctions accompanied by band bending, as shown in Fig. 7b. Upon exposure to NO_2 gas, which is known for its strong electron affinity and oxidative properties, electron extraction begins from the electron accumulation side of ZnO resulting in widening of the depletion layer, leading to an increase in the resistance of the heterojunctions. In the presence of dry air, oxygen molecules adhere to the surface, displacing the previously adsorbed NO_2 molecules. This leads to the release of electrons from trapped NO_2 molecules to SnO_2, ZnO, and the SnO_2-ZnO heterojunction and leads to a large increase in the conductivity of SnO_2-ZnO compared to the bare SnO_2 and ZnO.

Conclusions

Our study demonstrates the effectiveness of an MOF-derived SnO_2-ZnO sensor in detecting a wide range of NO_2 gas concentrations (25–100 ppm). The mole ratio of Zn to Sn was adjusted for optimal NO_2 gas detection, and Sn/Zn with a molar ratio of 1/0.50 provided the maximum response (R_g/R_a) of 7.37 to 100 ppm of NO_2 gas at the optimized operating temperature of 225°C. The response and recovery times of the SZ 1–0.50 sensor were 100 s and 440 s, respectively. Additionally, it exhibits good cyclability, selectivity, and long-term stability. These outcomes underscore the importance of advancing MOF-derived metal oxide semiconductors in the realm of NO_2 gas sensing, offering heightened selectivity, stability, and endurance. Consequently, our research contributes significantly to the progress of affordable gas sensors, with potential

applications spanning from industrial sectors to healthcare settings.

Acknowledgments The authors would like to thank MRC MNIT Jaipur for the characterization facilities.

Conflict of interest The authors declare that there is no conflict of interest that they have no known competing financial interests or personal relationships that could have appeared to influence the work reported in this paper.

References

1. X. Wang, N. Ding, S.D. Harlow, J.F. Randolph, E.B. Gold, C. Derby, H.M. Kravitz, G. Greendale, X. Wu, K. Ebisu, J. Schwartz, and S.K. Park, Associations between exposure to air pollution and sex hormones during the menopausal transition. *Sci. Total. Environ.* 908, 168317 (2024).
2. W. Li and W. Wang, Causal effects of exposure to ambient air pollution on cancer risk: insights from genetic evidence. *Sci. Total. Environ.* 912, 168843 (2024).
3. L. Xu, R. Xu, Y. Ye, R. Wang, J. Wei, C. Shi, Q. Lin, Z. Lv, S. Huang, Q. Tian, and Y. Liu, Short-term exposure to ambient air pollution and hospital admissions for angina among older adults in South China. *Atmos. Environ.* 318, 120198 (2024).
4. K. Supphapipat, P. Leurcharusmee, N. Chattipakorn, and S.C. Chattipakorn, Impact of air pollution on postoperative outcomes following organ transplantation: evidence from clinical investigations. *Clin. Transplant.* 38, 1 (2023).
5. OMS, WHO global air quality guidelines, Part. Matter (PM2.5 PM10), Ozone, Nitrogen Dioxide, Sulfur Dioxide Carbon Monoxide (2021). pp. 1–360
6. National Ambient Air Quality Standards, (n.d.). https://pcb.assam.gov.in/information-services/national-ambient-air-quality-standards
7. G.J.M. Velders, G.P. Geilenkirchen, and R. de Lange, Higher than expected NOx emission from trucks may affect attainability of NO_2 limit values in the Netherlands. *Atmos. Environ.* 45, 3025 (2011).
8. S.C. Anenberg, J. Miller, R. Minjares, L. Du, D.K. Henze, F. Lacey, C.S. Malley, L. Emberson, V. Franco, Z. Klimont, and C. Heyes, Impacts and mitigation of excess diesel-related NO_x emissions in 11 major vehicle markets. *Nature* 545, 467 (2017).
9. Q. Li, W. Zeng, and Y. Li, Metal oxide gas sensors for detecting NO_2 in industrial exhaust gas: recent developments. *Sens. Actuators B Chem.* 359, 131579 (2022).
10. S.W. Lee, W. Lee, Y. Hong, G. Lee, and D.S. Yoon, Recent advances in carbon material-based NO_2 gas sensors. *Sens. Actuators B Chem.* 255, 1788 (2018).
11. C. Zhang, Y. Luo, J. Xu, and M. Debliquy, Room temperature conductive type metal oxide semiconductor gas sensors for NO_2 detection. *Sens. Actuators A Phys.* 289, 118 (2019).
12. N. Karmakar, R. Fernandes, S. Jain, U.V. Patil, N.G. Shimpi, N.V. Bhat, and D.C. Kothari, Room temperature NO_2 gas sensing properties of p-toluenesulfonic acid doped silver-polypyrrole nanocomposite. *Sens. Actuators B Chem.* 242, 118 (2017).
13. X. Zhou, Z. Xue, X. Chen, C. Huang, W. Bai, Z. Lu, and T. Wang, Nanomaterial-based gas sensors used for breath diagnosis. *J. Mater. Chem. B* 8, 3231 (2020).
14. G. Drera, S. Freddi, A.V. Emelianov, I.I. Bobrinetskiy, M. Chiesa, M. Zanotti, S. Pagliara, F.S. Fedorov, A.G. Nasibulin, P. Montuschi, and L. Sangaletti, Exploring the performance of a functionalized CNT-based sensor array for breathomics through clustering and classification algorithms: from gas sensing of selective biomarkers to discrimination of chronic obstructive pulmonary disease. *RSC Adv.* 11, 30270 (2021).
15. R.K. Sonker, S.R. Sabhajeet, S. Singh, and B.C. Yadav, Synthesis of ZnO nanopetals and its application as NO_2 gas sensor. *Mater. Lett.* 152, 189 (2015).
16. P.H. Suman, A.A. Felix, H.L. Tuller, J.A. Varela, and M.O. Orlandi, Comparative gas sensor response of SnO_2, SnO and Sn_3O_4 nanobelts to NO_2 and potential interferents. *Sens. Actuators B Chem.* 208, 122 (2015).
17. D. Han, L. Zhai, F. Gu, and Z. Wang, Highly sensitive NO_2 gas sensor of ppb-level detection based on In_2O_3 nanobricks at low temperature. *Sens. Actuators B Chem.* 262, 655 (2018).
18. B. Liu, X. Liu, Z. Yuan, Y. Jiang, Y. Su, J. Ma, and H. Tai, A flexible NO_2 gas sensor based on polypyrrole/nitrogen-doped multiwall carbon nanotube operating at room temperature. *Sens. Actuators B Chem.* 295, 86 (2019).
19. Y. Seekaew, D. Phokharatkul, and A. Wisitsoraat, Applied surface science highly sensitive and selective room-temperature NO_2 gas sensor based on bilayer transferred chemical vapor deposited graphene. *Appl. Surf. Sci.* 404, 357 (2017).
20. S. Novikov, N. Lebedeva, A. Satrapinski, J. Walden, V. Davydov, and A. Lebedev, Graphene based sensor for environmental monitoring of NO_2. *Sens. Actuators B Chem.* 236, 1054 (2016).
21. X.T. Yin, W.D. Zhou, J. Li, Q. Wang, F.Y. Wu, D. Dastan, D. Wang, H. Garmestani, X.M. Wang, and Ş Ţălu, A highly sensitivity and selectivity Pt-SnO_2 nanoparticles for sensing applications at extremely low level hydrogen gas detection. *J. Alloys Compd.* 805, 229 (2019).
22. Y.L.T. Ngo and S.H. Hur, Low-temperature NO_2 gas sensor fabricated with NiO and reduced graphene oxide hybrid structure. *Mater. Res. Bull.* 84, 168 (2016).
23. H. Bai, H. Guo, J. Wang, Y. Dong, B. Liu, Z. Xie, F. Guo, D. Chen, R. Zhang, and Y. Zheng, A room-temperature NO_2 gas sensor based on CuO nanoflakes modified with rGO nanosheets. *Sens. Actuators B Chem.* 337, 129783 (2021).
24. S.D. Lawaniya, S. Kumar, Y. Yu, H.-G. Rubahn, Y.K. Mishra, and K. Awasthi, Functional nanomaterials in flexible gas sensors: recent progress and future prospects. *Mater. Today Chem.* 29, 101428 (2023).
25. Y. Zhu, J. Dong, G. Li, C. Liu, Q. Xie, L. Wang, L.J. Wang, and M. You, Bilayer polymer dielectric systems for high response NO_2 gas sensors. *Mater. Lett.* 288, 129370 (2021).
26. A. Umar, A.A. Ibrahim, H. Algadi, H. Albargi, M.A. Alsairi, Y. Wang, and S. Akbar, Enhanced NO_2 gas sensor device based on supramolecularly assembled polyaniline/silver oxide/graphene oxide composites. *Ceram. Int.* 47, 25696 (2021).
27. G.H. Jain, MOS gas sensors: What determines our choice?, in 2011 Fifth International Conference on Sensing Technology. (IEEE, 2011). pp. 66–72
28. A. Afzal, N. Cioffi, L. Sabbatini, and L. Torsi, NO_x sensors based on semiconducting metal oxide nanostructures: progress and perspectives. *Sens. Actuators B Chem.* 171–172, 25 (2012).
29. L.Y. Jian, H.Y. Lee, and C.T. Lee, Surface morphology-dependent sensitivity of thin-film-structured indium oxide-based NO_2 gas sensors. *J. Electron. Mater.* 48, 2391 (2019).
30. S.T. Shishiyanu, T.S. Shishiyanu, and O.I. Lupan, Sensing characteristics of tin-doped ZnO thin films as NO_2 gas sensor. *Sens. Actuators B Chem.* 107, 379 (2005).
31. J. Zhao, T. Yang, Y. Liu, Z. Wang, X. Li, Y. Sun, Y. Du, Y. Li, and G. Lu, Enhancement of NO_2 gas sensing response based on ordered mesoporous Fe-doped In_2O_3. *Sens. Actuators B Chem.* 191, 806 (2014).
32. M. Penza, C. Martucci, and G. Cassano, NOx gas sensing characteristics of WO_3 thin films activated by noble metals (Pd, Pt, Au) layers. *Sens. Actuators B Chem.* 50, 52 (1998).

33. T. Li, Y. Shen, X. Zhong, S. Zhao, G. Li, B. Cui, D. Wei, and K. Wei, Effect of noble metal element on microstructure and NO_2 sensing properties of WO_3 nanoplates prepared from a low-grade scheelite concentrate. *J. Alloys Compd.* 818, 152927 (2020).
34. J. Kim, M. Nazarian-Samani, J. Lee, S. Kil Lee, J.H. Pi, K.H. Lee, Y.J. Kim, S. Lee, and W. Lee, Extrinsic oxygen defects in SnO/SnO_2 heterostructure for efficient NO_2 gas detection. *Sens. Actuators B Chem.* 399, 134751 (2024).
35. J.H. Kim, J.H. Lee, A. Mirzaei, H.W. Kim, and S.S. Kim, SnO_2(n)-NiO(p) composite nanowebs: gas sensing properties and sensing mechanisms. *Sens. Actuators B Chem.* 258, 204 (2018).
36. P.H. Phuoc, N.N. Viet, L.V. Thong, C.M. Hung, N.D. Hoa, N. Van Duy, H.S. Hong, and N. Van Hieu, Comparative study on the gas-sensing performance of ZnO/SnO_2 external and ZnO-SnO_2 internal heterojunctions for ppb H_2S and NO_2 gases detection. *Sens. Actuators B Chem.* 334, 129606 (2021).
37. Y. Cheng, T. Shao, J. Dong, H. Kou, F. Zhang, J. Guo, and X. Liu, MOF-derived SnO_2@ZnO ethanol sensors with enhanced gas sensing properties. *Vacuum* 216, 112440 (2023).
38. J. Xiao, K. Diao, Z. Zheng, and X. Cui, MOF-derived porous ZnO/Co_3O_4 nanocomposites for high performance acetone gas sensing. *J. Mater. Sci. Mater. Electron.* 29, 8535 (2018).
39. Z. Li, Y. Zhang, H. Zhang, Y. Jiang, and J. Yi, Superior NO_2 sensing of MOF-derived indium-doped ZnO porous hollow cages. *ACS Appl. Mater. Interfaces* 12, 37489 (2020).
40. A. Sharma, K. Karuppasamy, D. Vikraman, Y. Cho, K. Adaikalam, J.G. Korvink, H.S. Kim, and B. Sharma, Metal organic framework-derived ZnO@GC nanoarchitecture as an effective hydrogen gas sensor with improved selectivity and gas response. *ACS Appl. Mater. Interfaces* 14, 44516 (2022).
41. S. Venkateshalu, G. Subashini, P. Bhardwaj, G. Jacob, R. Sellappan, B. Abdullah, M. Al Alwan, M. Khaloofah, M. Al Alodhayb, M. Khalid, and A. Nirmala, Phosphorene, antimonene, silicene and siloxene based novel 2D electrode materials for supercapacitors—a brief review. *J. Energy Storage* 48, 104027 (2022).
42. D. Zhang, Z. Yang, S. Yu, Q. Mi, and Q. Pan, Diversiform metal oxide-based hybrid nanostructures for gas sensing with versatile prospects. *Coord. Chem. Rev.* 413, 213272 (2020).
43. P.M. Bulemo and J.Y. Cheong, MOF-derived SnO_2 hollow spheres for acetone gas sensing. *J. Mater. Sci. Mater. Electron.* 34, 1 (2023).
44. X. Ren, Z. Xu, D. Liu, Y. Li, Z. Zhang, and Z. Tang, Conductometric NO_2 gas sensors based on MOF-derived porous ZnO nanoparticles. *Sens. Actuators B Chem.* 357, 131384 (2022).
45. H. Zhang, S. Guo, W. Zheng, H. Wang, H.Y. Li, M.H. Yu, Z. Chang, X.H. Bu, and H. Liu, Facile engineering of metal–organic framework derived SnO_2-ZnO composite based gas sensor toward superior acetone sensing performance. *Chem. Eng. J.* 469, 143927 (2023).
46. L. Guo, F. Chen, N. Xie, X. Kou, C. Wang, Y. Sun, F. Liu, X. Liang, Y. Gao, X. Yan, T. Zhang, and G. Lu, Ultra-sensitive sensing platform based on Pt-ZnO-In_2O_3 nanofibers for detection of acetone. *Sens. Actuators B Chem.* 272, 185 (2018).
47. S. Kumar, S.D. Lawaniya, S. Agarwal, Y.T. Yu, S.R. Nelamarri, M. Kumar, Y.K. Mishra, and K. Awasthi, Optimization of Pt nanoparticles loading in ZnO for highly selective and stable hydrogen gas sensor at reduced working temperature. *Sens. Actuators B Chem.* 375, 132943 (2023).
48. G. Pandey, S.D. Lawaniya, S. Kumar, P.K. Dwivedi, and K. Awasthi, A highly selective, efficient hydrogen gas sensor based on bimetallic (Pd-Au) alloy nanoparticle (NP)-decorated SnO_2 nanorods. *J. Mater. Chem. A* 11, 26687 (2023).
49. G. Pandey, M. Bhardwaj, S. Kumar, S.D. Lawaniya, M. Kumar, P.K. Dwivedi, and K. Awasthi, Synergistic effects of Pd-Ag decoration on SnO/SnO_2 nanosheets for enhanced hydrogen sensing. *Sens. Actuators B Chem.* 402, 135062 (2024).
50. S. Kumar, S.D. Lawaniya, S.R. Nelamarri, M. Kumar, P.K. Dwivedi, Y.-T. Yu, Y.K. Mishra, and K. Awasthi, Bimetallic Ag-Pd nanoparticles decorated ZnO nanorods for efficient hydrogen sensing. *Sens. Actuators B Chem.* 394, 134394 (2023).
51. S. Kumar, S.D. Lawaniya, S.R. Nelamarri, M. Kumar, P.K. Dwivedi, Y.K. Mishra, and K. Awasthi, ZnO nanosheets decorated with Ag-Pt nanoparticles for selective detection of ethanol. *ACS Appl. Nano Mater.* 6, 15479 (2023).
52. M. Verma, P.K. Dwivedi, and B. Das, Structure–property correlation of pure and Sn-doped ZnO nanocrystalline materials prepared by co-precipitation. *J. Exp. Nanosci.* 10, 438 (2015).
53. X. Ren, Z. Xu, Z. Zhang, and Z. Tang, Enhanced NO_2 sensing performance of ZnO-SnO_2 heterojunction derived from metal-organic frameworks. *Nanomaterials* 12, 1 (2022).
54. S.D. Lawaniya, S. Kumar, Y. Yu, and K. Awasthi, Ammonia sensing properties of PPy nanostructures (urchins/flowers) towards low-cost and flexible gas sensors at room temperature. *Sens. Actuators B Chem.* 382, 133566 (2023).
55. S. Robbiani, B.J. Lotesoriere, R.L. Dellacà, and L. Capelli, Physical confounding factors affecting gas sensors response: a review on effects and compensation strategies for electronic nose applications. *Chemosensors* 11, 514 (2023).
56. P.M. Bulemo and J.Y. Cheong, Review on porosity control in nanostructured semiconducting metal oxides and its influence on chemiresistive gas sensing. *ACS Appl. Nano Mater.* 6, 1027 (2023).
57. X. Wang, Y. Wang, F. Tian, H. Liang, K. Wang, X. Zhao, Z. Lu, K. Jiang, L. Yang, and X. Lou, From the surface reaction control to gas-diffusion control: the synthesis of hierarchical porous SnO_2 microspheres and their gas-sensing mechanism. *J. Phys. Chem. C* 119, 15963 (2015).
58. V.V. Deshmane and A.V. Patil, Synergy of semiconductor (Hematite) & catalytic (Ni) properties enhance gas sensing behavior to NO_2. *Mater. Res. Express.* 6, 075910 (2019).
59. T.H. Han, S.Y. Bak, S. Kim, S.H. Lee, Y.J. Han, and M. Yi, Decoration of CuO NWs gas sensor with ZnO NPs for improving NO_2 sensing characteristics. *Sensors* 21, 1 (2021).
60. N. Ramgir, R. Bhusari, N.S. Rawat, S.J. Patil, A.K. Debnath, S.C. Gadkari, and K.P. Muthe, TiO_2/ZnO heterostructure nanowire based NO_2 sensor. *Mater. Sci. Semicond. Process.* 106, 104770 (2020).
61. W. Zeng, Y. Liu, J. Mei, C. Tang, K. Luo, S. Li, H. Zhan, and Z. He, Hierarchical SnO_2-Sn_3O_4 heterostructural gas sensor with high sensitivity and selectivity to NO_2. *Sens. Actuators B Chem.* 301, 127010 (2019).
62. Y.H. Navale, S.T. Navale, F.J. Stadler, N.S. Ramgir, and V.B. Patil, Enhanced NO_2 sensing aptness of ZnO nanowire/CuO nanoparticle heterostructure-based gas sensors. *Ceram. Int.* 45, 1513 (2019).
63. C.W. Zou, J. Wang, and W. Xie, Synthesis and enhanced NO_2 gas sensing properties of ZnO nanorods/TiO_2 nanoparticles heterojunction composites. *J. Colloid Interface Sci.* 478, 22 (2016).
64. Z. Zhang, M. Xu, L. Liu, X. Ruan, J. Yan, W. Zhao, J. Yun, Y. Wang, S. Qin, and T. Zhang, Novel SnO_2@ZnO hierarchical nanostructures for highly sensitive and selective NO_2 gas sensing. *Sens. Actuators B Chem.* 257, 714 (2018).
65. S. Zhao, Y. Shen, R. Maboudian, C. Carraro, C. Han, W. Liu, and D. Wei, Facile synthesis of ZnO-SnO_2 hetero-structured nanowires for high-performance NO_2 sensing application. *Sens. Actuators B Chem.* 333, 129613 (2021).
66. V.T. Duoc, C.M. Hung, H. Nguyen, N. Van Duy, N. Van Hieu, and N.D. Hoa, Room temperature highly toxic NO_2 gas sensors

based on rootstock/scion nanowires of SnO_2/ZnO, ZnO/SnO_2, SnO_2/SnO_2 and ZnO/ZnO. *Sens. Actuators B Chem.* 348, 130652 (2021).